

Article

Effect of Oxidant Concentration on Properties of Ferrite Films by Spin-Spray Deposition

Hai Liu ^{1,2,*}, Jihong Liao ², Gang Huang ³, Xiaona Jiang ¹, Zhong Yu ¹, Zhongwen Lan ¹ and Ke Sun ¹ 

¹ School of Materials and Energy, University of Electronic Science and Technology of China, Chengdu 610054, China

² Hubei Key Laboratory of Low Dimensional Optoelectronic Materials and Devices, Hubei University of Arts and Science, Xiangyang 441053, China

³ Hubei Huaci Electronic Technology Co., Ltd., Xiangyang 441053, China

* Correspondence: xiaomingever@gmail.com

Abstract: In response to the demands for high frequency, miniaturization, and high integration in electronic devices, such as inductors and DC-DC converters, nickel–zinc ferrite thin films exhibit significant application value and development potential. For regulating the magnetic properties and microstructure of spin-sprayed polycrystalline ferrite materials, a comprehensive understanding of the impact of oxidant concentration on film reaction is essential. This study finds that as the concentration of the NaNO₂ oxidant increases, the grain size of the nickel–zinc ferrite thin film samples progressively enlarges. Due to the preferential occupation of iron ions at the B sites, the saturation magnetization correspondingly increases. However, when the oxidant concentration becomes excessive, the preferential (222) orientation growth of the film is disrupted, leading to the agglomeration and uneven growth of grains, transitioning from triangular plate-like to spherical in shape. This increase in grain size alters the magnetization mechanism of the thin film, predominantly favoring domain wall movement. Upon analyzing the microstructure and magnetic characteristics, it becomes evident that the concentration of oxidant is a key determinant in the spin-spray deposition process.

Keywords: magnetic thin film; spin-spray deposition; ferrite; oxidant concentration



Citation: Liu, H.; Liao, J.; Huang, G.; Jiang, X.; Yu, Z.; Lan, Z.; Sun, K. Effect of Oxidant Concentration on Properties of Ferrite Films by Spin-Spray Deposition. *Coatings* **2024**, *14*, 120. <https://doi.org/10.3390/coatings14010120>

Academic Editor: Gianni Barucca

Received: 19 December 2023

Revised: 9 January 2024

Accepted: 12 January 2024

Published: 16 January 2024



Copyright: © 2024 by the authors. Licensee MDPI, Basel, Switzerland. This article is an open access article distributed under the terms and conditions of the Creative Commons Attribution (CC BY) license (<https://creativecommons.org/licenses/by/4.0/>).

1. Introduction

In contemporary electronic systems, system-on-chip (SoC) technology is pivotal for enhancing device frequencies, achieving miniaturization, and ensuring robust reliability and multifunctionality. Thin film inductors integral to SoCs are essential in AC electronic and radio devices for oscillators, choke coils, filters, and impedance matching [1–7]. SoCs confront challenges in inductor design: air-core planar inductors with inadequate inductance density and suboptimal high-frequency performance, and metal magnetic thin films as inductor cores suffering from high-frequency inefficiencies due to low resistivity and significant eddy current losses.

Ferrite magnetic thin films emerge as a viable alternative, marked by higher resistivity, offering reduced high-frequency eddy current losses and broader magnetic circuit design adaptability. However, studies indicate that conventional deposition methods like sputtering and vacuum evaporation are incompatible with semiconductor process integration due to the high-temperature annealing process required for the crystallization of ferrite thin films [8–10]. Addressing these issues requires developing new low-temperature deposition techniques. Innovations in spin-spray deposition appear promising, enabling the crystallization of soft magnetic ferrite thin films at lower temperatures (≤ 130 °C), which are compatible with semiconductor processes [11–14]. This method not only reduces energy consumption but also maintains superior high-frequency magnetic performance [15–17].

Therefore, developing soft magnetic ferrite thin films with high magnetic permeability, high saturation magnetization, and high resistivity, compatible with semiconductor pro-

cesses, is critical to meet the demands of SoCs for high inductance values and application frequencies in advanced electronic systems. In this field of spin-spray deposition study, Obi innovatively approached the fabrication of $\text{Ni}_{0.27}\text{Zn}_x\text{Fe}_{2.73-x}\text{O}_4$ thin films [18–20]. Employing a spin-spraying deposition technique on glass substrates under a 360 Oe magnetic field, Obi successfully produced these films. A critical step involved adjusting the pH values of the metallate and oxidant solutions, significantly influencing the microstructure and magnetic properties of the films. The findings indicated that these films achieved a magnetic permeability of 50 at 1 GHz, demonstrating remarkable magnetic performance. Following Obi's work, Ray further delved into the deposition process of ferrite thin films, exploring various parameters. Ray proposed a μ -droplet deposition regime, which, compared to the continuous liquid layer regime, exhibited superior performance in terms of Snoek's product. Optimal results were obtained using an oxidant with a pH of 8.28 [21].

Furthermore, Matsushita's research also found that incorporating FeCl_3 into the primary formulation resulted in coarser grain growth, leading to a wavy appearance on the film's surface; cross-sectional images revealed that the grains in these films grew in a columnar structure. These studies underscore the importance of precursor solution and pH value control in the fabrication process of NiZn ferrite thin films [22–24]. Precise control of the chemical reaction conditions can significantly enhance the microstructure and magnetic properties of the films, thus offering materials with higher performance for high-frequency electromagnetic applications.

As a pivotal aspect of the reaction process, the role of the oxidant has not been systematically investigated. Recognizing this gap, this study embarked on an experimental analysis of oxidant concentration. It delves into the impact of oxidant concentration on the reaction dynamics as well as its regulatory effect on the microstructural morphology and magnetic properties of the resultant materials.

2. Materials and Methods

A series of NaNO_2 solutions with varying concentrations of 1, 2, 3, 4, and 5 mmol/L, respectively, and a 20 mmol/L CH_3COONa oxidizing solution were prepared. Additionally, aqueous solutions of NiCl_2 , ZnCl_2 , and FeCl_2 were synthesized. Both types of solutions were simultaneously sprayed onto a 0.2 mm glass substrate using an ultrasonic nebulizer nozzle. The substrate was then fixed on a rotating heating plate using a vacuum pneumatic suction cup. Heat the setup to 120 °C to fabricate a ferrite thin film of $\text{Ni}_{0.34}\text{Zn}_{0.16}\text{Fe}_{2.50}\text{O}_4$, and the reaction time for each sample was maintained at 20 min.

The characterization of ferrite thin films employed a suite of advanced techniques, each contributing unique insights into their structural, magnetic, and physical attributes, thus aiding future optimization efforts. The structural properties were probed using X-ray diffraction (XRD), utilizing a Shimadzu Maxima-X XRD-7000 equipped with $\text{Cu-K}\alpha$ radiation, offering detailed crystallographic information. For microstructural imaging, Scanning Electron Microscopy (FESEM) was applied, specifically using a JEOL JSM-7800F, to obtain high-resolution surface morphology. Magnetic characterization was conducted at room temperature using a Vibrating Sample Magnetometer (Lake Shore 8604), including hysteresis loop measurements, revealing key magnetic properties. The deposition process's thermal dynamics were monitored via a Fotric 220 series thermal camera, ensuring precise control over temperature conditions. Additionally, permeability spectrum analysis was conducted using an Agilent N5227A PNA network analyzer, paired with a fixture based on the shorted microstrip method, enabling the assessment of electromagnetic properties [25,26]. Finally, Atomic Force Microscopy (AFM) was performed using an MFP-3D Infinity AFM, which provided nanoscale topographical details.

3. Results

Figure 1 illustrates the X-ray diffraction (XRD) patterns of nickel–zinc ferrite thin films deposited under different oxidant concentrations. These patterns reveal the crystallization of the films, as evidenced by the distinct peaks characteristic of typical spinel structures. As

the concentration of the oxidant increases, the relative peak intensity remains essentially unchanged. To estimate the average crystallite diameters (d) of five different specimens, the Scherrer formula was employed [27,28], which is expressed as shown below.

$$L = \frac{0.9\lambda}{\beta \cos \theta} \quad (1)$$

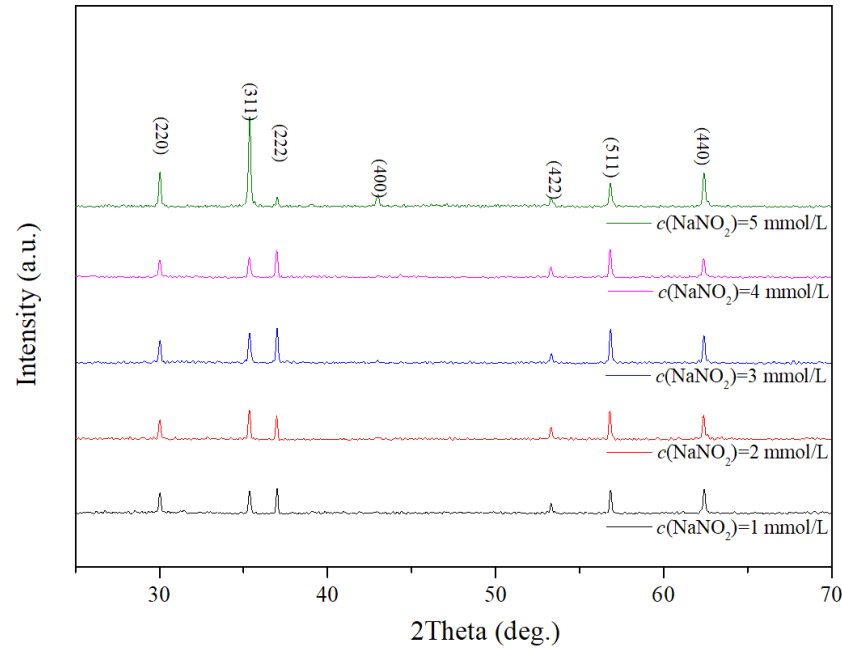


Figure 1. X-ray diffraction results of spin-sprayed films with different oxidant concentrations.

Here, λ represents the wavelength of $\text{CuK}\alpha$ radiation (0.15408 nm), θ is the Bragg angle, and β is the corrected full-width at half-maximum (FWHM). However, the diffraction results reveal that the thin film material exhibits a single, sharp spinel pure phase. A change is observed only when the oxidant concentration reaches 5 mmol/L. The most notable changes are the weakening of the (222) plane peak and the strengthening of the (311) main peak.

To elucidate the particular (222) preferential orientation, a schematic diagram of the spinel ferrite crystal structure is presented in Figure 2. The size of the spheres at different crystallographic sites in the diagram is set for aesthetic purposes only and does not represent the actual ionic radii. As shown, the silver spheres represent the A-site sublattice, which are the eight tetrahedral sites; the gold spheres represent the B-site sublattice, which are the 16 octahedral sites. The dense stacking plane (hkl) of O^{2-} and B-site cations is highlighted with dashed lines. This dense packing plane satisfies $h = k = l$. The inter-planar spacing (d) of a cubic crystal can be straightforwardly calculated using its lattice constant (a), which is the length of the crystal's edge. By inserting this value into Formula (2) specifically for calculating the inter-planar spacing in cubic crystals, we find that the resulting value of h (Miller index) is equal to 2.

$$d = \frac{a}{\sqrt{h^2 + k^2 + l^2}} \quad (2)$$

As evidenced by X-ray diffraction, ferrite grains growing with the (222) plane parallel to the substrate constitute a significant portion of the film composition. Theoretically, the crystallographic plane (222) orientation should be denoted as the [111] crystallographic direction orientation. To confirm the existence of this (222) crystallographic plane preferential orientation, which will result in a triangular grain shape, the micro-morphologies of all samples were characterized using FESEM and are presented in Figure 3.

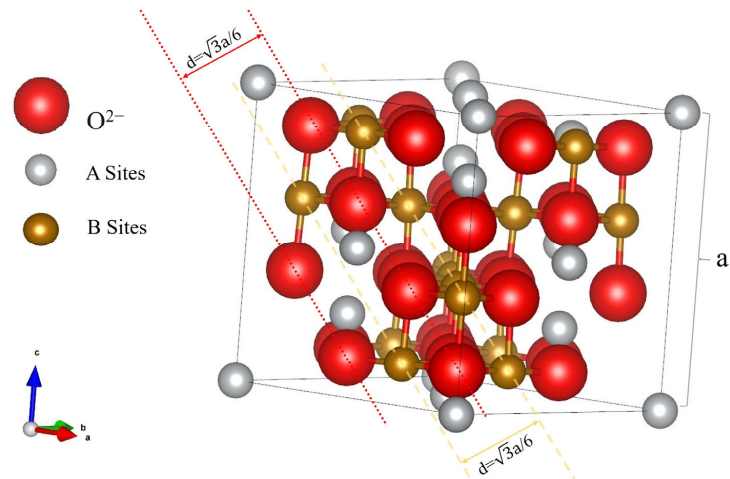


Figure 2. Crystal structure of the spinel ferrite.

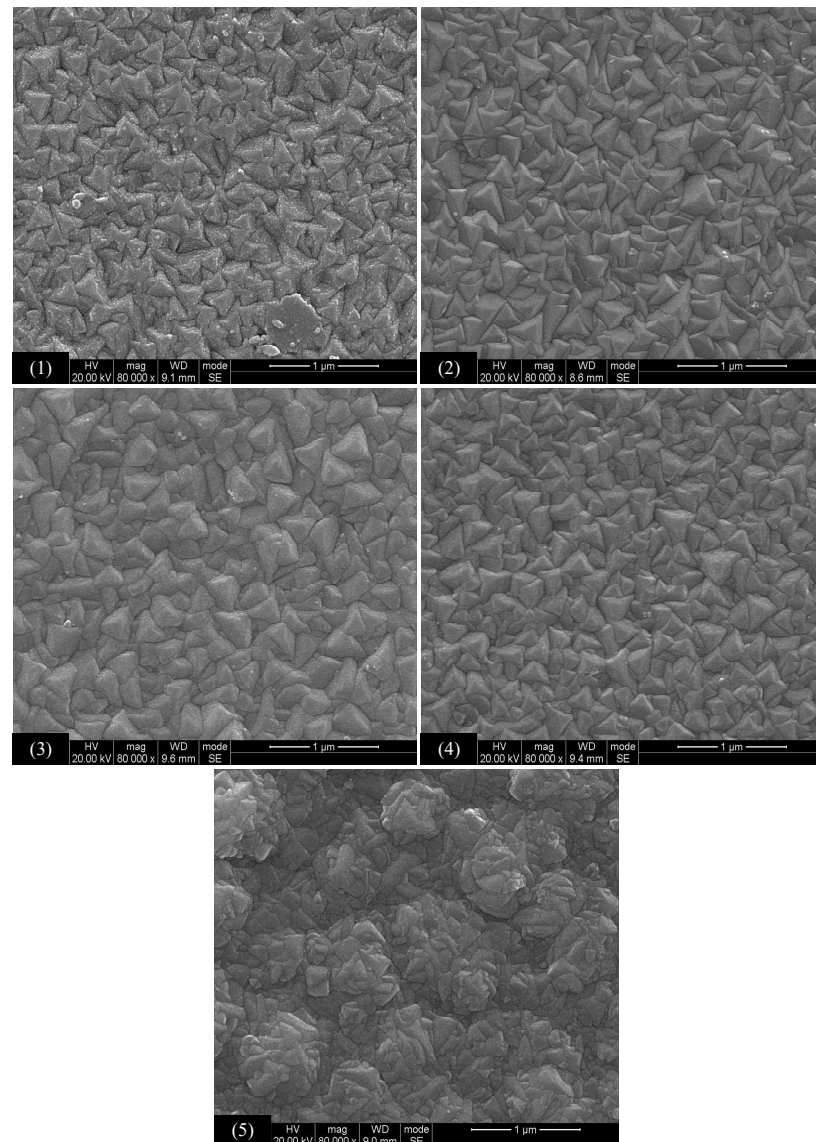


Figure 3. FESEM images of ferrite thin film samples at various NaNO_2 concentrations. (1) $c(\text{NaNO}_2) = 1 \text{ mmol/L}$; (2) $c(\text{NaNO}_2) = 2 \text{ mmol/L}$; (3) $c(\text{NaNO}_2) = 3 \text{ mmol/L}$; (4) $c(\text{NaNO}_2) = 4 \text{ mmol/L}$; (5) $c(\text{NaNO}_2) = 5 \text{ mmol/L}$.

To evaluate the degree of orientation, the predominance of the (222) facet was quantified using the Lotgering factor [29–31]:

$$f_L = \frac{P - P_0}{1 - P_0} \quad (3)$$

where $P = \frac{\sum I_{(222)}}{\sum I_{(hkl)}}$ is the Lotgering factor value for samples with a (222) preferred orientation and $P_0 = \frac{\sum I_{0(222)}}{\sum I_{0(hkl)}}$ denotes the factor for those with a random orientation. XRD peaks within the 2θ range of 20° – 70° were employed for this calculation. The computed (222)-facet proportions for the samples, which were represented by the aforementioned Lotgering factor, were found to be 1.15, 0.82, 1.12, 1.36, and 0.16, respectively. Notably, samples possessing a preferred orientation demonstrated a narrower grain size distribution, which was indicative of more uniform grains. The diminished intensity of the (222) peak points to a decrease in preferential orientation growth in these materials. Key parameters such as the lattice constant (a), average grain size (D) calculated using Scherrer's formula, and the deposition rate of the thin film calculated by dividing the film thickness by 20 min are summarized in Table 1.

Table 1. Parameters of spin-sprayed ferrite thin films with different oxidant concentrations.

NaNO ₂ (mmol/L)	a (Å)	D (nm)	Deposition Rate (nm/min)
1	8.41	48 ± 9	32
2	8.41	54 ± 11	35
3	8.41	95 ± 9	43
4	8.41	57 ± 7	46
5	8.41	71 ± 21	42

Figure 3 shows the scanning electron microscopy (SEM) results of ferrite thin film samples under different oxidant concentrations. An increase in the oxidant concentration leads to significant changes in the micro-morphology of the films. When the NaNO₂ concentration is between 1 and 4 mmol/L, the films exhibit a distinct triangular plate-like grain structure. At concentrations of 1 to 3 mmol/L, the grains are observed to grow larger, indicating that an increase in oxidant content promotes grain growth. At a NaNO₂ concentration of 5 mmol/L, the micro-morphology transitions from a uniform distribution of triangular grains to a state of grain agglomeration with noticeable surface undulations on the grains.

Except for sample 5, the other thin film deposited on the glass substrate displayed triangular grains. This specific morphology is in harmony with the (222) preferred orientation identified earlier. Considering that a cross-sectional view along the (hhh) crystal plane of a cubic crystal typically exhibits a triangular shape, the emergence of triangular grains in these films can be logically deduced.

The distinct (222) facet orientation and triangular grain structure observed in the ferrite thin films provide crucial insights into their growth kinetics during spin-spray deposition at the atomic level. This understanding resolves ambiguities about the spin-spray film deposition mechanism and supports previous theories about ferrite thin film development [32]. The formation process begins as the substrate captures ferrous ions from the sprayed droplets, which then interact with OH[−] ions. Heating and oxidation, facilitated by NO₂[−], transform these ions into trivalent iron ions (B sites) accompanied by the dehydration of neighboring OH[−] ions, thus forming the second layer of the film. This process leaves unoccupied oxygen bonds, prompting the absorption of new cations for subsequent layer formation, thus sustaining the cycle. Other cations, occupying A sites, are also integrated into this compact spinel ferrite structure, which is a process guided by the principle of minimum energy utilization.

Figure 4 presents the hysteresis loops of NiZn ferrite thin film samples under different oxidant concentrations with the samples' saturation magnetization (M_s) and coercivity listed in Table 2. Based on the definition of saturation magnetization (the sum of magnetic moments per unit volume), the magnetization of ferrites is primarily determined by the material's magnetic moments and density. According to the film growth mechanism of spin spraying (with preferential dense packing of (222) planes), B-site ferric ions predominantly participate in the oxidation reaction on the (222) planes. At lower oxidant concentrations, an increase in the oxidant concentration leads to a rise in the content of B-site iron ions, thereby enhancing the net magnetic moment and increasing the material's saturation magnetization, M_s , which reaches its maximum at a NaNO_2 concentration of 3 mmol/L. As the growth of the spin-sprayed NiZn ferrite thin film is primarily driven by layer-by-layer reaction sequences propelled by the oxidation of B-site ions, these ions preferentially participate in the oxidation reactions. When the concentration exceeds 3 mmol/L, the oxidation reaction of the B-site ferric ions becomes sufficiently complete, leading to a gradual weakening of the (222) preferential orientation resulting from the stacking growth of the B-site sublattice. Moreover, the grains begin to show significant agglomeration and non-uniform growth, resulting in a decrease in the density of the ferrite thin film, thereby reducing the saturation magnetization.

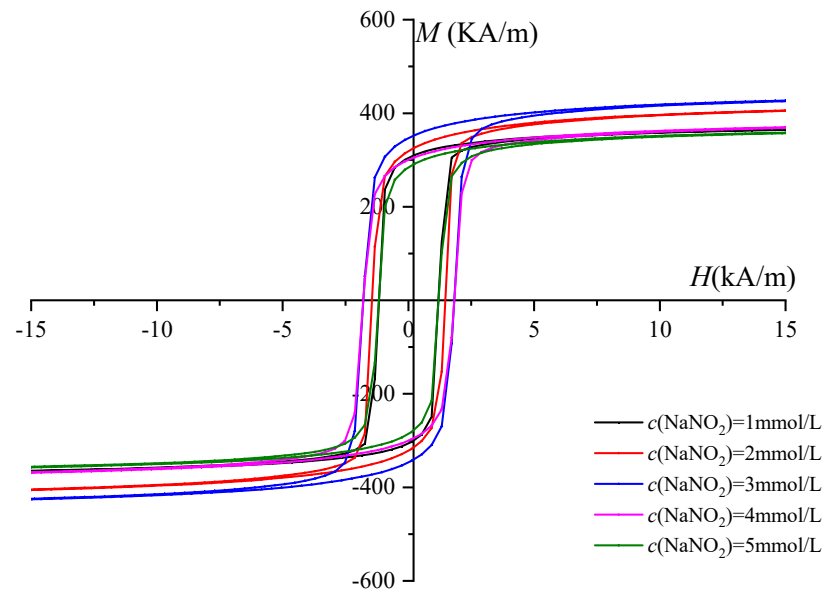


Figure 4. Hysteresis loops of the spin-sprayed ferrite thin film of different oxidant concentrations.

Table 2. Magnetic properties of ferrite thin film samples at different NaNO_2 concentrations.

$c(\text{NaNO}_2)$ (mmol/L)	1	2	3	4	5
M_s (kA/m)	384	432	454	393	380
H_c (kA/m)	1.11	1.59	1.91	1.83	1.03

Coercivity in ferrite thin films, an extrinsic property, displays complex variations across samples. A trend of coercivity (H_c) aligns with microstructure changes, as explained by the random anisotropy model. The coercive force in these films is theoretically linked to the relationship between exchange length (L_{ex}) and grain size (d), underscoring the intricate interplay between microstructure and magnetic behavior.

(i) Small grain size ($D < L_{ex}$):

$$H_c = \frac{K_1^4 d^6}{\mu_0 M_s A^3}; \quad (4)$$

(ii) Large grain size ($D > L_{ex}$):

$$H_c = \frac{(AK_1)^{1/2}}{\mu_0 M_s d}. \quad (5)$$

The exchange length (L_{ex}), a pivotal parameter in magnetic materials, is mathematically defined as $L_{ex} = (A/K_1)^{1/2}$, where A represents the exchange stiffness and K_1 denotes the anisotropic constant [33,34]. This expression encapsulates the fundamental interplay between these two key properties. The observed increasing trend in coercivity (H_c) with the increase in grain size across the samples implicates that they all fall into the scenario where the grain size (D) is smaller than the exchange length ($D > L_{ex}$). This relationship serves as a critical indicator of the magnetic behavior of the samples, linking microstructural characteristics to magnetic properties.

It is important to emphasize that variations in the micromorphology of the material can substantially influence its permeability, which in turn affects the cutoff frequency. This critical relationship is elucidated in Figure 5, which displays the permeability spectra of four distinct specimens. In this figure, both the real and imaginary components of the permeability are delineated separately, providing a comprehensive view of the material's electromagnetic response across the frequency range. This detailed representation facilitates a deeper understanding of how microstructural changes impact the electromagnetic properties of the material, thereby offering valuable insights for material design and application.

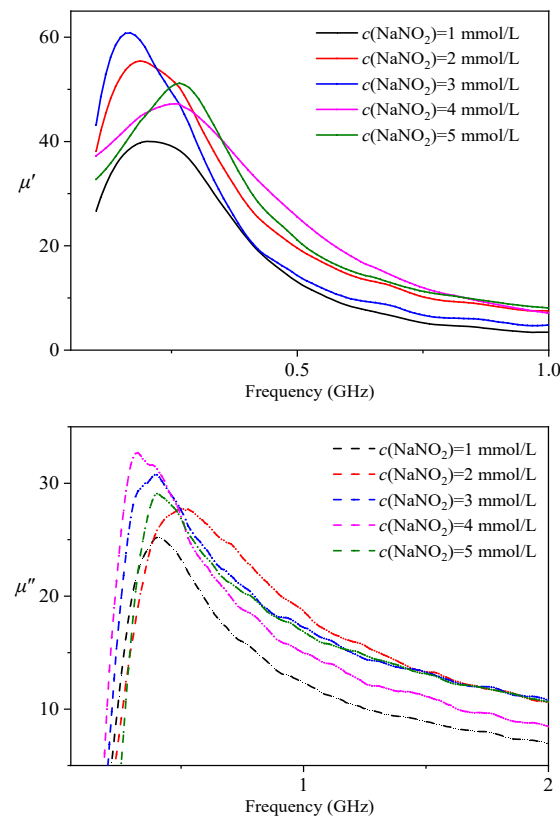


Figure 5. Magnetic permeability spectra of ferrite thin films with different NaNO_2 concentrations.

Figure 5 shows the magnetic spectra of ferrite thin films at different oxidant concentrations, and the real parts μ' and imaginary parts μ'' are shown in two panels separately, with the corresponding magnetic permeability and cutoff frequency results listed in Table 3. As the concentration of NaNO_2 increases, the magnetic permeability also increases, reaching its maximum at 3 mmol/L. Thereafter, the magnetic permeability decreases, which is consistent with the trend observed in the saturation magnetization as a function of NaNO_2 concentration.

Table 3. Magnetic permeability spectrum data of ferrite thin films at different oxidant concentrations.

$c(\text{NaNO}_2)$ (mmol/L)	μ'_{\max}	f_r (MHz)
1	40	401
2	55	482
3	61	375
4	48	265
5	53	367

The Acher equation posits a fundamental relationship in magnetic materials, asserting that the maximum real part of permeability shares an inverse proportionality with the cutoff frequency, as cited in the references [35,36]. This study delves into two primary magnetization mechanisms: domain rotation and domain wall motion. These mechanisms demonstrate distinct patterns of variation in relation to grain size. Specifically, the study reveals that (1) domain rotation $\mu_i \approx \frac{\mu_0 M_s^2}{3(K)}$ and (2) domain wall motion $\mu_i \approx \frac{\mu_0 M_s^2 A^3}{K_1^4 D^6}$ both exhibit an inverse correlation with grain size, as detailed in the references, which is a trend that aligns with observations made in coercivity measurements.

Moreover, it is noteworthy that under equivalent conditions, the domain wall motion mechanism results in a permeability value that is threefold higher than that produced by domain rotation. This disparity becomes particularly relevant as the grain size increases, potentially leading to a transition in the microstructure from a single magnetic domain to a multi-domain configuration. Such a transition alters the predominant magnetization mechanism, thereby influencing the material's magnetic properties.

In the context of our study, this phenomenon elucidates the observed magnetic behavior of the samples. Notably, the sample with the oxidation of $c(\text{NaNO}_2) = 3$ mmol/L shows a less pronounced reduction in magnetic permeability for considerably larger grains. This outcome can be attributed to the differential impact of grain size on the two magnetization mechanisms, underscoring the complex interplay between microstructure and magnetic properties in thin film materials.

4. Conclusions

The analysis of magnetic properties and microstructure suggests that oxidant concentration plays a critical role in influencing the spin-spray deposition process. As the concentration of NaNO_2 oxidant increases, the grain size of the thin film samples progressively enlarges, and the saturation magnetization also rises due to the preferential occupation of iron ions at the B sites. However, when the oxidant concentration becomes excessive, the (222) preferential orientation growth of the film is disrupted. This disruption leads to agglomeration and an uneven growth of the grains with the grains transitioning from triangular plate-like to spherical in shape. The increase in grain size alters the magnetization mechanism of the thin film, predominantly favoring domain wall movement.

Author Contributions: Conceptualization, H.L.; Data curation, H.L.; Investigation, X.J.; Methodology, G.H. and J.L.; Project administration, Z.Y.; Supervision, K.S.; Writing—original draft, H.L.; Writing—review and editing, Z.Y. and Z.L. All authors have read and agreed to the published version of the manuscript.

Funding: We thank the Research and Development Projects in Xiangyang City (project number 2022ABH006835) for funding.

Institutional Review Board Statement: Not applicable.

Informed Consent Statement: Not applicable.

Data Availability Statement: Data are contained within the article.

Conflicts of Interest: Author Gang Huang was employed by the company Hubei Huaci Electronic Technology Co., Ltd. The remaining authors declare that the research was conducted in the absence of any commercial or financial relationships that could be construed as a potential conflict of interest.

References

1. Hao, A.; Ismail, M.; He, S.; Qin, N.; Huang, W.; Wu, J.; Bao, D. Improved Unipolar Resistive Switching Characteristics of Au-Doped Nickel Ferrite Magnetic Thin Films for Nonvolatile Memory Applications. *J. Alloys Compd.* **2018**, *732*, 573–584. [[CrossRef](#)]
2. Abdellatif, M.H.; Azab, A.A.; Moustafa, A.M. Dielectric Spectroscopy of Localized Electrical Charges in Ferrite Thin Film. *J. Electron. Mater.* **2018**, *47*, 378–384. [[CrossRef](#)]
3. Harris, V.G. Modern Microwave Ferrites. *IEEE Trans. Magn.* **2012**, *48*, 1075–1104. [[CrossRef](#)]
4. Sahu, B.N.; Venkataramani, N.; Prasad, S.; Krishnan, R. Effect of Thickness on Magnetic and Microwave Properties of RF-Sputtered Zn-Ferrite Thin Films. *AIP Adv.* **2017**, *7*, 056102. [[CrossRef](#)]
5. Chen, Z.; Harris, V.G. Ferrite Film Growth on Semiconductor Substrates towards Microwave and Millimeter Wave Integrated Circuits. *J. Appl. Phys.* **2012**, *112*, 081101. [[CrossRef](#)]
6. Huang, W.; Zhou, J.; Froeter, P.; Walsh, K.; Liu, S.; Michaels, J.; Li, M.; Gong, S.; Li, X. CMOS-Compatible on-Chip Self-Rolled-up Inductors for RF/Mm-Wave Applications. In Proceedings of the 2017 IEEE MTT-S International Microwave Symposium (IMS), Honolulu, HI, USA, 4–9 June 2017; IEEE: Honolulu, HI, USA, 2017; pp. 1645–1648.
7. Coll, M.; Montero Moreno, J.M.; Gazquez, J.; Nielsch, K.; Obradors, X.; Puig, T. Low Temperature Stabilization of Nanoscale Epitaxial Spinel Ferrite Thin Films by Atomic Layer Deposition. *Adv. Funct. Mater.* **2014**, *24*, 5368–5374. [[CrossRef](#)]
8. Narang, S.B.; Pubby, K. Nickel Spinel Ferrites: A Review. *J. Magn. Magn. Mater.* **2021**, *519*, 167163. [[CrossRef](#)]
9. Vinosha, P.A.; Manikandan, A.; Judith Ceicilia, A.S.; Dinesh, A.; Francisco Nirmala, G.; Preetha, A.C.; Slimani, Y.; Almessiere, M.A.; Baykal, A.; Xavier, B. Review on Recent Advances of Zinc Substituted Cobalt Ferrite Nanoparticles: Synthesis Characterization and Diverse Applications. *Ceram. Int.* **2021**, *47*, 10512–10535. [[CrossRef](#)]
10. Darwish, M.A.; Trukhanov, A.V.; Senatov, O.S.; Morchenko, A.T.; Saafan, S.A.; Astapovich, K.A.; Trukhanov, S.V.; Trukhanova, E.L.; Pilyushkin, A.A.; Sombra, A.S.B.; et al. Investigation of AC-Measurements of Epoxy/Ferrite Composites. *Nanomaterials* **2020**, *10*, 492. [[CrossRef](#)] [[PubMed](#)]
11. Abe, M.; Tamaura, Y. Ferrite Plating in Aqueous Solution: New Technique for Preparing Magnetic Thin Film. *J. Appl. Phys.* **1984**, *55*, 2614–2616. [[CrossRef](#)]
12. Abe, M.; Tada, M.; Matsushita, N.; Shimada, Y. Phenomenological Theory of Permeability in Films Having No In-Plane Magnetic Anisotropy: Application to Spin-Sprayed Ferrite Films. *J. Appl. Phys.* **2006**, *99*, 08M907. [[CrossRef](#)]
13. Liu, H.; Yu, Z.; Fu, B.; Ran, M.; Wu, C.; Jiang, X.; Guo, R.; Lan, Z.; Sun, K. Anisotropic Growth and Magnetic Properties of Nickel-Zinc Ferrite Thin Film by Spin Spray Deposition. *Ceram. Int.* **2021**, *47*, 1318–1324. [[CrossRef](#)]
14. Emori, S.; Gray, B.A.; Jeon, H.-M.; Peoples, J.; Schmitt, M.; Mahalingam, K.; Hill, M.; McConney, M.E.; Gray, M.T.; Alaan, U.S.; et al. Coexistence of Low Damping and Strong Magnetoelastic Coupling in Epitaxial Spinel Ferrite Thin Films. *Adv. Mater.* **2017**, *29*, 1701130. [[CrossRef](#)]
15. Ran, M.; Yu, Z.; Sun, K.; Wu, C.; Qing, H.; Liu, H.; Lan, Z.; Jiang, X. Effects of Aqueous Ethanol Solutions on the Structural and Magnetic Properties of NiZn Ferrite Thin Films Prepared by Spin-Spray Deposition. *Ceram. Int.* **2021**, *47*, 15520–15526. [[CrossRef](#)]
16. Ko, S.W.; Li, J.; Podraza, N.J.; Dickey, E.C.; Trolrier-McKinstry, S. Spin Spray-Deposited Nickel Manganite Thermistor Films For Microbolometer Applications. *J. Am. Ceram. Soc.* **2011**, *94*, 516–523. [[CrossRef](#)]
17. Zhou, Z.; Obi, O.; Nan, T.X.; Beguhn, S.; Lou, J.; Yang, X.; Gao, Y.; Li, M.; Rand, S.; Lin, H.; et al. Low-Temperature Spin Spray Deposited Ferrite/Piezoelectric Thin Film Magnetolectric Heterostructures with Strong Magnetolectric Coupling. *J. Mater. Sci. Mater. Electron.* **2014**, *25*, 1188–1192. [[CrossRef](#)]
18. Obi, O.; Liu, M.; Lou, J.; Stoute, S.; Xing, X.; Sun, N.X.; Warzywoda, J.; Sacco, A.; Oates, D.E.; Dionne, G.F. Spin-Spray Deposited NiZn-Ferrite Films Exhibiting $\mu_r' > 50$ at GHz Range. *J. Appl. Phys.* **2011**, *109*, 07E527. [[CrossRef](#)]
19. Wang, X.; Zhou, Z.; Behugn, S.; Liu, M.; Lin, H.; Yang, X.; Gao, Y.; Nan, T.; Xing, X.; Hu, Z.; et al. Growth Behavior and RF/Microwave Properties of Low Temperature Spin-Sprayed NiZn Ferrite. *J. Mater. Sci. Mater. Electron.* **2015**, *26*, 1890–1894. [[CrossRef](#)]
20. Li, M.; Zhou, Z.; Liu, M.; Lou, J.; Oates, D.E.; Dionne, G.F.; Wang, M.L.; Sun, N.X. Novel NiZnAl-Ferrites and Strong Magnetolectric Coupling in NiZnAl-Ferrite/PZT Multiferroic Heterostructures. *J. Phys. D Appl. Phys.* **2013**, *46*, 275001. [[CrossRef](#)]
21. Mirzaee, S.; Farjami Shayesteh, S.; Mahdavi, S.; Hekmatara, S.H. Synthesis, Characterization and Monte Carlo Simulation of CoFe₂O₄/Polyvinylpyrrolidone Nanocomposites: The Coercivity Investigation. *J. Magn. Magn. Mater.* **2015**, *393*, 1–7. [[CrossRef](#)]
22. Salcedo Rodríguez, K.L.; Bridoux, G.; Heluani, S.P.; Pasquevich, G.A.; Esquinazi, P.D.; Rodríguez Torres, C.E. Influence of Substrate Effects in Magnetic and Transport Properties of Magnesium Ferrite Thin Films. *J. Magn. Magn. Mater.* **2019**, *469*, 643–649. [[CrossRef](#)]
23. Oujja, M.; Martín-García, L.; Rebollar, E.; Quesada, A.; García, M.A.; Fernández, J.F.; Marco, J.F.; de la Figuera, J.; Castillejo, M. Effect of Wavelength, Deposition Temperature and Substrate Type on Cobalt Ferrite Thin Films Grown by Pulsed Laser Deposition. *Appl. Surf. Sci.* **2018**, *452*, 19–31. [[CrossRef](#)]

24. Pradhan, D.K.; Kumari, S.; Pradhan, D.K.; Kumar, A.; Katiyar, R.S.; Cohen, R.E. Effect of Substrate Temperature on Structural and Magnetic Properties of C-Axis Oriented Spinel Ferrite $\text{Ni}_{0.65}\text{Zn}_{0.35}\text{Fe}_2\text{O}_4$ (NZFO) Thin Films. *J. Alloys Compd.* **2018**, *766*, 1074–1079. [[CrossRef](#)]
25. Wu, Y.; Tang, Z.; Xu, Y.; Zhang, B.; He, X. A New Shorted Microstrip Method to Determine the Complex Permeability of Thin Films. *IEEE Trans. Magn.* **2010**, *46*, 886–888. [[CrossRef](#)]
26. Li, Y.F.; Li, E.; Zhang, Y.P.; Zhao, C.; Yang, T. Ultra-Wideband Variable Temperature Measurement System for Complex Permeability of Magnetic Thin Film $\text{Fe}_{66}\text{Co}_{17}\text{B}_{16}\text{Si}_1$. *IEEE Trans. Magn.* **2018**, *54*, 1–7. [[CrossRef](#)]
27. Nawle, A.C.; Humbe, A.V.; Babrekar, M.K.; Deshmukh, S.S.; Jadhav, K.M. Deposition, Characterization, Magnetic and Optical Properties of Zn Doped CuFe_2O_4 Thin Films. *J. Alloys Compd.* **2017**, *695*, 1573–1582. [[CrossRef](#)]
28. Brabers, V.A.M. Chapter 3 Progress in Spinel Ferrite Research. In *Handbook of Magnetic Materials*; Elsevier: Amsterdam, The Netherlands, 1995; Volume 8, pp. 189–324.
29. Yang, S.; Chen, F.; Gao, X.; Shen, Q.; Zhang, L. Enhanced Power Factor of Textured Al-Doped-ZnO Ceramics by Field-Assisted Deforming. *J. Am. Ceram. Soc.* **2017**, *100*, 1300–1305. [[CrossRef](#)]
30. Wu, C.; Wang, W.; Li, Q.; Wei, M.; Luo, Q.; Fan, Y.; Jiang, X.; Lan, Z.; Jiao, Z.; Tian, Y.; et al. Barium Hexaferrites with Narrow Ferrimagnetic Resonance Linewidth Tailored by Site-Controlled Cu Doping. *J. Am. Ceram. Soc.* **2022**, *105*, 7492–7501. [[CrossRef](#)]
31. Kitayama, M.; Hirao, K.; Toriyama, M.; Kanzaki, S. Thermal Conductivity of $\text{SS-Si}_3\text{N}_4$: I, Effects of Various Microstructural Factors. *J. Am. Ceram. Soc.* **1999**, *82*, 3105–3112. [[CrossRef](#)]
32. Taniguchi, A.; Taniguchi, T.; Wagata, H.; Katsumata, K.; Okada, K.; Matsushita, N. Liquid-Phase Atomic Layer Deposition of Crystalline Hematite without Post-Growth Annealing. *CrystEngComm* **2019**, *21*, 4184–4191. [[CrossRef](#)]
33. Alben, R.; Becker, J.J.; Chi, M.C. Random Anisotropy in Amorphous Ferromagnets. *J. Appl. Phys.* **1978**, *49*, 1653–1658. [[CrossRef](#)]
34. Herzer, G. Anisotropies in Soft Magnetic Nanocrystalline Alloys. *J. Magn. Magn. Mater.* **2005**, *294*, 99–106. [[CrossRef](#)]
35. Zhang, Y.; Dai, B.; Li, J.; Zhu, H.; Zhu, X.; Li, X.; Ren, J.; Ren, Y. Break the Acher’s Limit: Improve Both Resonance Frequency and Initial Permeability in Patterned FeNi Strip Film. *J. Alloys Compd.* **2017**, *725*, 598–605. [[CrossRef](#)]
36. Jin, H.; Miyazaki, T. Soft Magnetism. In *The Physics of Ferromagnetism*; Miyazaki, T., Jin, H., Eds.; Springer Series in Materials Science; Springer: Berlin/Heidelberg, Germany, 2012; pp. 305–338. ISBN 978-3-642-25583-0.

Disclaimer/Publisher’s Note: The statements, opinions and data contained in all publications are solely those of the individual author(s) and contributor(s) and not of MDPI and/or the editor(s). MDPI and/or the editor(s) disclaim responsibility for any injury to people or property resulting from any ideas, methods, instructions or products referred to in the content.